



Immersed boundary finite elements for 3D flow simulations in twin-screw extruders



J.-F. Héту, F. Ilinca *

National Research Council, 75 de Mortagne, Boucherville, Qc, Canada J4B 6Y4

ARTICLE INFO

Article history:

Received 28 February 2012

Received in revised form 12 June 2012

Accepted 19 June 2012

Available online 24 July 2012

Keywords:

Immersed boundary method

Twin-screw extruders

Finite elements

Non-body-conformal mesh

Body conformal enrichment

ABSTRACT

This paper presents applications of a recently proposed Immersed Boundary (IB) method to the solution of the flow around moving and complex shaped surfaces, in particular inside twin-screw extruders. Solving the flow around rotating screw elements implies significant changes in the computational topology at every time step. Using multiple meshes or adaptive methods to tackle these would require extensive meshing and interpolation work that has to be repeated each time step. Mesh generation and solution interpolation between successive grids may be costly and may introduce errors if the geometry changes significantly during the course of the computation. These drawbacks are avoided when the solution algorithm can tackle grids that do not fit the shape of immersed objects. In this work a fixed mesh is used covering both the fluid and solid regions, and the boundary of immersed objects is defined using a time dependent level-set function. The Body Conformal Enrichment (BCE) method is used to accurately impose boundary conditions on the surface of immersed bodies. The proposed algorithm enriches the finite element discretization of interface elements with additional degrees of freedom, the latter being eliminated at element level. Numerical applications are shown in which the flow inside twin-screw extruders is computed for multiple screw elements. A generalized non-Newtonian fluid is used to model molten polymer. Solutions will be shown for various rotation velocities of the screw as the viscosity depends on the shear rate.

Crown Copyright © 2012 Published by Elsevier Ltd. All rights reserved.

1. Introduction

CFD solvers generally use body-conformal (BC) grids (i.e. the external boundary and surfaces of immersed solids are represented by the mesh faces), but there is an increased interest in solution algorithms for non-body-conformal grids. For these methods the spatial discretization is done over a single domain containing both fluid and solid regions and where mesh points are not necessarily located on the fluid–solid interface [1–3]. Immersed Boundary (IB) methods have the main advantage of avoiding costly and sometimes very difficult meshing work on body-fitted geometries. Instead, a simple geometry is meshed with a relatively uniform grid. The IB method results also in important algorithmic simplifications when moving immersed bodies are considered. One important drawback of such a method is that the boundary which has an important influence on the solution is also a place where distorted elements may be found once regular mesh elements are cut by the solid boundary. This challenge can be overcome by the use of stabilized finite elements which provide stable accurate solutions even on highly stretched or distorted meshes. The imposition of

the boundary conditions on the immersed boundary is also a point of concern which will be addressed here by the Body Conformal Enrichment (BCE) method. The procedure consists in adding degrees of freedom associated to fluid/solid interface nodes that are latter eliminated at element level.

The goal of the present work is the solution by means of the IB-BCE finite element method proposed in [4–6] of flows in presence of moving and complex shaped solid surfaces as those encountered in the case of co-rotating twin-screw extruders. Screw extruders are widely used in the plastic industry to plasticize polymers, i.e. to increase their temperature up to a desired value for injection molding applications, and to achieve a desired degree of mixing by distributing and dispersing the polymer compounds. Twin screw extruders are commonly used and they are classified by the rotation direction of each screw (co-rotating and counter-rotating), the degree of intermeshing and the type of screw elements. For co-rotating screw extruders three types of elements are widely used: the full flight screw, the kneading blocks and the screw mixing element consisting of a standard screw profile with slots cut across the flight tip to increase the flow leakage.

Efficient application of twin-screw extruders requires characterization of the mixing behavior of various screw elements, a task that can be tackled efficiently by numerical simulation. First attempts to simulate twin screw extruders addressed only a 2D

* Corresponding author. Tel.: +1 450 641 5072; fax: +1 450 641 5106.

E-mail address: florin.ilinca@nrc-nrc.gc.ca (F. Ilinca).

analogy of the flow [7–9]. Bertrand et al. [10] presented a fictitious domain method based on a mesh refinement technique overlapping a single reference mesh. The mesh was locally adapted to enrich the discretization in small gaps and applications were shown for 2D flow simulation in twin-screw extruders. Kajiwara et al. [8] developed a 3D numerical technique to simulate fluid flow in the case of full flight conveying screw elements. Their simulations were however restricted to one section of the analysis domain, located in the nip region, and relied upon periodic boundary conditions. Cheng and Manas-Zloczower [11,12] and Yao and Manas-Zloczower [13] reported 3D numerical studies of co-rotating twin screw extruders using the commercial software FIDAP. Their approach was based on selecting a number of sequential geometries representing various positions of the screws in order to represent a complete cycle and then computing steady state solutions for each of them. Zhang et al. [14] used a mesh superposition technique to solve intermeshing twin-screw extruders without remeshing. The procedure, incorporated into the Polyflow software, generates finite element meshes for the flow domain and each screw element, respectively, which are then superimposed. The position of each screw is then updated at each time step. Three-dimensional solutions of the steady state flow and energy equations inside twin-screw extruders are reported by Ishikawa et al. [15]. The Stokes equations describing the polymer flow are solved separately for each flow domain corresponding to successive positions of the screw. The same approach is applied to the energy equation by including the convective term but neglecting the transient effects. One drawback of such an approach is that while the polymer melt may reach a quasi-steady state (or periodic variation), the heat transfer should take into account the coupling between the convective transport and the actual change in the flow domain. Therefore, the steady state solution of the energy equation should only be seen as an approximation of the global heat balance inside the screw extruder. Kalyon and Malik [16,17] used the same steady-state framework to describe the flow and heat transfer of generalized Newtonian fluids inside co-rotating and counter-rotating twin screw extruders. Their studies investigate the pressure distribution inside combinations of multiple screw elements and inside screwdie configurations.

The main hurdle when modeling the flow inside twin-screw extruders is the continuous change in the computational domain determined by the rotation of the screws. On the other hand, a simplifying behavior is that inertia is negligible for molten polymers. This results in flow solutions depending only on the conditions at the current time step. At this point, almost all numerical simulations of 3D twin-screw extruders were performed using a sequence of steady-state solutions on different meshes representing the successive positions of the screws. Such an approach is not complicated in terms of 3D flow solution, but instead forces the use of more complicated solution techniques when flow solutions should be transferred from one time step to the next as is the case for particle tracking algorithms. Moreover, such approaches are not appropriate if one need to solve the energy or other scalar transport equations for which the inertia cannot be neglected.

In the present work we use an IB method solving the equations on a mesh that does not represent the screw surfaces. A comparison of body-fitted, embedded and immersed boundary techniques using the same flow solver is presented in [3]. In most IB methods, boundary conditions on immersed surfaces are handled either accurately by using dynamic data structures to add/remove grid points as needed [18,19] or in an approximate way by imposing the boundary conditions to the grid point closest to the surface or through least-squares [20]. Our recently proposed approach [4] achieves the level of accuracy of cut cell dynamic node addition techniques with none of their drawbacks (increased CPU time and costly dynamic data structures). This approach was extended to

moving fluid/solid interfaces in Ref. [5]. For problems involving convective transport, the proposed IB method was shown to predict adequately the flow structures produced by the continuous repositioning of the solid surfaces [21]. The use of a single mesh facilitates the solution of transport phenomena as those encountered for particle tracking and residence time computations.

The paper is organized as follows. First the model problem and the associated finite element formulation are presented. The IB formulation and the procedure to impose the boundary conditions on moving solid surfaces are discussed briefly. Section 3 illustrates the application of the IB method to 3-D co-rotating twin-screw extruders. The paper ends with conclusions.

2. The model problem

We consider the transient incompressible fluid flow problem on a bounded computational domain Ω formed by the fluid region $\Omega_f(t)$ and the solid volume $\Omega_s(t)$ as shown in Fig. 1. The fluid and solid volumes are time dependent but the total volume Ω formed by their reunion is not. The immersed interface $\Gamma_i(t) = \partial\Omega_f(t) \cap \partial\Omega_s(t)$ represents a boundary for the fluid flow and is considered as being time dependent.

2.1. Model equations and boundary conditions

The flow of molten polymers is dominated by viscous forces and the inertia can be neglected. Therefore the flow is described by the incompressible Stokes equations:

$$0 = -\nabla p + \nabla \cdot [\eta(\nabla \mathbf{u} + (\nabla \mathbf{u})^T)], \quad (1)$$

$$\nabla \cdot \mathbf{u} = 0, \quad (2)$$

where \mathbf{u} the velocity vector, p the pressure and η the viscosity.

The interface Γ_i , between the fluid and solid regions, is specified using a level-set function ψ , which is defined as a signed distance function from the immersed interface:

$$\psi(\mathbf{x}, t) = \begin{cases} d(\mathbf{x}, \mathbf{x}_i(t)), & \mathbf{x} \text{ in the fluid region,} \\ 0, & \mathbf{x} \text{ on the fluid/solid interface,} \\ -d(\mathbf{x}, \mathbf{x}_i(t)), & \mathbf{x} \text{ in the solid region,} \end{cases} \quad (3)$$

where $d(\mathbf{x}, \mathbf{x}_i(t))$ is the distance between the point $P(\mathbf{x})$ and the fluid/solid interface $P_i(\mathbf{x}_i(t))$ at time t . Hence, points in the fluid region have positive values of ψ , whereas points in the solid region have negative ones. The boundary conditions associated to Eqs. (1) and (2) are

$$\mathbf{u} = \mathbf{U}_D(\mathbf{x}, t), \quad \text{for } \mathbf{x} \in \Gamma_D(t), \quad (4)$$

$$\eta(\nabla \mathbf{u} + \nabla \mathbf{u}^T) \cdot \hat{\mathbf{n}} - p \hat{\mathbf{n}} = \mathbf{t}(\mathbf{x}, t), \quad \text{for } \mathbf{x} \in \Gamma_t(t), \quad (5)$$

where Γ_D is the portion of the fluid boundary $\partial\Omega_f$ where Dirichlet conditions are imposed (including the moving immersed solid surfaces), and \mathbf{t} is the traction imposed on the remaining fluid

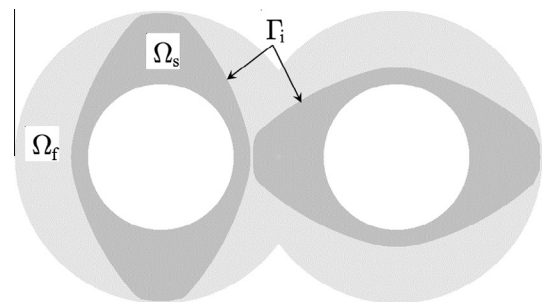


Fig. 1. Computational domain formed by fluid region $\Omega_f(t)$ and solid region $\Omega_s(t)$.

boundary $\Gamma_t = \partial\Omega_f \setminus \Gamma_D$. Dirichlet boundary conditions are imposed at the interface between fluid and solid regions, i.e. $\Gamma_i \subset \Gamma_D$. Because Γ_i is not represented by the finite element discretization, a special procedure is used to enforce velocity boundary conditions on this surface. This approach will be discussed in Section 2.4.

2.2. The finite element formulation

The finite element formulation is the same as in Ref. [5]. Both velocity and pressure are discretized using linear continuous interpolants and the weak form of the equations corresponds to the GLS (Galerkin Least-Squares) method:

$$\int_{\Omega} \eta(\nabla \mathbf{u} + \nabla \mathbf{u}^T) \cdot \nabla \mathbf{N}_u \, d\Omega - \int_{\Omega} p \nabla \mathbf{N}_u \, d\Omega = \int_{\Gamma_t} \mathbf{t} \mathbf{N}_u \, d\Gamma, \quad (6)$$

$$\int_{\Omega} \nabla \cdot \mathbf{u} \mathbf{N}_p \, d\Omega + \sum_K \int_{\Omega_K} (\nabla p) \tau (\nabla \mathbf{N}_p) \, d\Omega_K = 0, \quad (7)$$

where (\mathbf{u}, p) is the velocity–pressure solution and \mathbf{N}_u , \mathbf{N}_p are continuous, piece-wise linear test functions associated to the velocity and pressure equations. The Eq. (6) and the first integral in Eq. (7) correspond to the Galerkin formulation whereas the integral over the elements interior is the GLS stabilization terms. The stabilization parameter is computed as from Refs. [22,23]:

$$\tau = \frac{m_k h_K^2}{4\eta} \quad (8)$$

Here h_K is the size of the element K and m_k is a coefficient set to 1/3 for linear elements (see [22,24]).

Note that the viscosity in (6) and (8) depends on the velocity gradient resulting in nonlinear equations which are solved with a few Picard steps followed by Newton–Raphson iterations. The resulting linear systems are solved using iterative solvers as described in the next section.

2.3. Parallel implementation

The finite element method has been implemented in parallel. The partitioning of the mesh is based solely on the connectivity of the nodes using the automatic graph partitioning tool ParMETIS [25]. Elements with nodes belonging to multiple partitions are ghosted on all processors which compute and assemble the associated elementary systems.

The linear systems from Eqs. (6) and (7) are generated directly in parallel, assembled in sparse row formats [26], and solved using the bi-conjugate gradient stabilized (Bi-CGSTAB) algorithm of van der Vorst [27]. The global matrix and corresponding iteration vectors are partitioned by block rows, and a block diagonal preconditioner is used. For this, each processor first computes an incomplete LU factorization of the diagonal block of its row. On each iteration, Bi-CGSTAB requires two matrix–vector multiplications $\{y\} = [A]\{x\}$ by the global matrix which entails each processor sending and receiving parts of the vector $\{x\}$, and a sparse upper/lower triangular system solve on the local part of the vector $\{x\}$ which can be done strictly locally.

Although the block diagonal preconditioner is completely parallel and requires no inter-processor communication, with increasing numbers of processors it becomes less effective, making Bi-CGSTAB require more iterations for a given system. So although more processors make each iteration faster and cheaper, more iterations are required. If the block diagonal preconditioner fails, a block SOR and block SSOR algorithm can be applied as preconditioner. However, even the first of these provisions is rarely required for the GLS formulation.

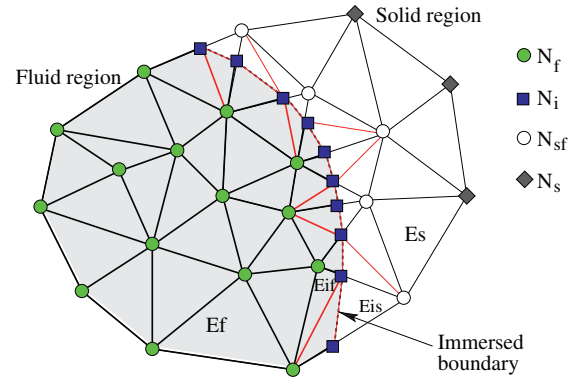


Fig. 2. Decomposition of elements cut by the immersed boundary.

2.4. The IB-BCE method

The algorithm used to treat the immersed boundary surface is the same as introduced by Ilinca and Hétu for the static fluid/solid interfaces [4] and for moving interfaces [5].

The mesh is intersected by the interface at the current time step t_n at points located along element edges (N_i in Fig. 2) and we consider those points as additional degrees of freedom in the finite element formulation. While elements cut by the immersed boundary have nodes in both fluid and solid regions, the addition of nodes on the interface and the decomposition of interface elements yields the formation of elements which are either entirely in the fluid region (E_{if} in Fig. 2) or in the solid region (E_{is} in Fig. 2).

When solving the fluid flow we consider that the solid embedded in the mesh has a prescribed velocity $\mathbf{u}_s(\mathbf{t})$, i.e. the screw velocity for twin-screw extruders. The solid velocity is therefore imposed on the additional interface nodes.

The pressure degrees of freedom are associated to the continuity equations. In order to enforce mass conservation in the entire fluid region, the continuity equations are solved on all fluid elements, including the fluid sub-elements at the interface. The continuity equations are not solved in the solid elements and the pressure is set to a constant (say zero) on solid nodes. The pressure discretization is considered discontinuous between interface sub-elements and the additional pressure degrees of freedom corresponding to interface nodes are eliminated by static condensation. For more details the reader should consult [4,5].

3. Applications

3.1. Flow around an array of spheres

The IB-BCE method is first demonstrated on the flow around spheres placed on a simple cubic lattice. This problem was previously used by the authors to validate the computation of the permeability coefficient in a porous media [6]. Details on the computational domain and boundary conditions could be found in [6]. The flow enters the computational domain at constant velocity U_0 and the distance between the center of adjacent spheres is L . Simulations were performed for various values of the sphere diameter D ranging between $0.2L$ and $1.3L$ resulting in a solid fraction of the bed of spheres varying between 4.19×10^{-3} and 0.896 . Computations were carried out in low Reynolds number regime ($Re = \rho U_0 L / \eta \ll 1$) for which the inertia in the momentum equations can be neglected [28]. The surface of the spheres on which no-slip boundary conditions are imposed is represented by a predetermined level-set function [6].

Computations were carried out for 3 meshes whose characteristics are given in Table 1. A cut through Mesh 2 corresponding to the

Table 1
Mesh characteristics for flow around an array of spheres.

Mesh	Element size	# Of nodes	# Of elements
1	$L/20$	62,181	280,000
2	$L/30$	202,181	940,000
3	$L/40$	472,361	2,240,000

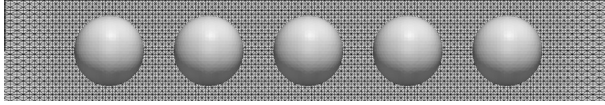


Fig. 3. Mesh 2 for $D = 0.7L$.

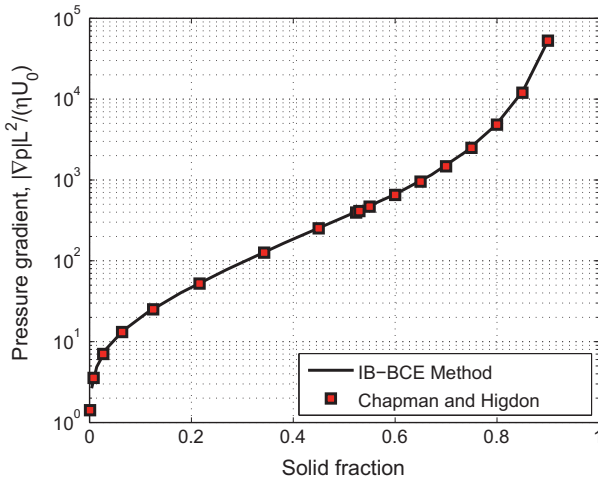


Fig. 4. Pressure gradient for the array of spheres.

mid-plane in the flow direction is shown in Fig. 3 for a diameter $D = 0.7L$. The mesh has 30 elements in directions transverse to the flow. As can be seen, the solid boundary of the spheres cuts through the elements, as the mesh is not constructed to fit the geometry of the immersed objects.

The dimensionless pressure gradient in the flow direction computed on Mesh 3 is shown in Fig. 4 as a function of the solid fraction. The results are compared with those of Chapman and Higdon [29]. Similar results were reported by Martys et al. [28] using a lattice Boltzmann method. As can be seen, the pressure drop increases with the solid fraction. The present numerical results are

Table 2
Screw configuration and flow parameters.

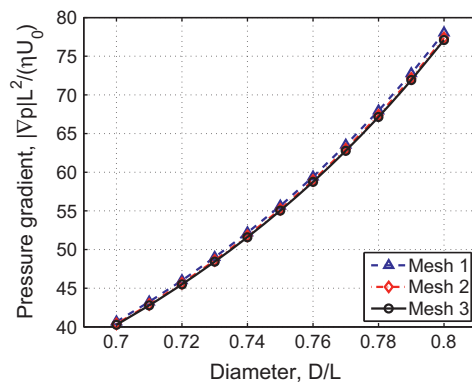
Case	Screw element type	Feed rate (kg/h)	Screw rotation speed (RPM)
A.1	Conveying	6.75	120
A.2	Conveying	3.375	120
A.3	Conveying	6.75	60
A.4	Conveying	6.75	240
B.1	Mixing	6.75	120
B.2	Mixing	3.375	120

in excellent agreement with those reported by Chapman and Higdon [29].

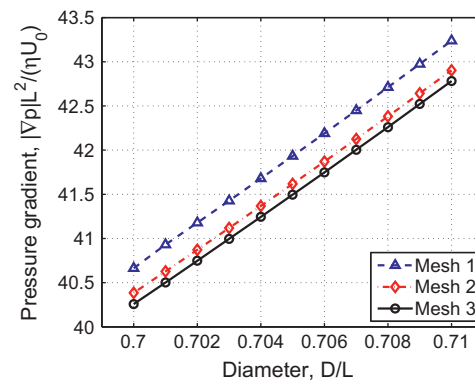
In the present IB-BCE method the boundary conditions on the fluid/solid interface are imposed with the same accuracy as if the mesh was body-conformal. Thus, the method is very sensitive to the position of the solid boundary inside mesh elements. Note that because the finite element method uses linear interpolation functions, the boundary is represented by planar surfaces inside mesh elements. However, the same would have been when using a body-conformal mesh. Thus, the accuracy with which the boundary is represented depends on the local mesh size. In order to assess the sensitivity of the IB-BCE method to changes in the location of the solid boundary within a mesh element, computations were carried out by varying the spheres diameter from $0.7L$ to $0.8L$ with a constant increment of $0.01L$. The results are plotted in Fig. 5a. Furthermore, very small changes in the location of the solid boundary were simulated by considering the diameter in the range between $0.7L$ and $0.71L$ with constant increments of $0.001L$. Recall that the mesh size is $0.05L$ for Mesh 1 and $0.025L$ for Mesh 3, which means that each change in the radius of the spheres determines a displacement of the interface with a distance 50–100 times smaller than the element size. The results from this set of computations are shown in Fig. 5b. As can be seen, the present numerical method is able to represent accurately even extremely small changes in the location of the immersed boundary. Note also that changes between the solutions on different meshes are small; 1% difference between the solutions on meshes 1 and 3 and only 0.2% difference between the solutions on meshes 2 and 3.

3.2. Flow around conveying and mixing twin-screw elements

In this section the IB solution algorithm is used to solve the flow around twin-screw elements. Two different configurations are studied containing either conveying or mixing elements. The screw configurations and flow parameters considered are summarized in Table 2. Reference conditions are A.1 and B.1 for the conveying and mixing elements respectively and then, solutions are obtained for



(a) Diameter increments of $0.01L$



(b) Diameter increments of $0.001L$

Fig. 5. Pressure gradient for small changes in sphere diameter.

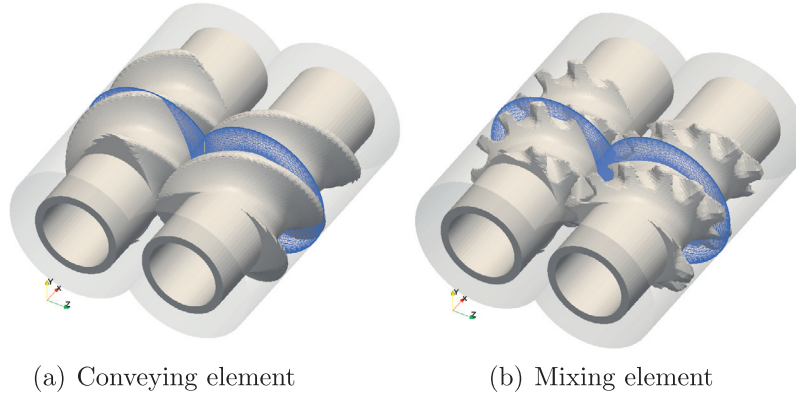


Fig. 6. Computational domain for screw elements.

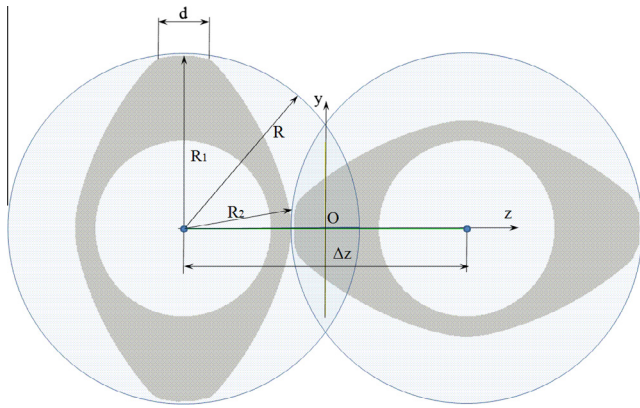


Fig. 7. Screw geometry for conveying element.

either different feed rate (A.2 and B.2) or different screw rotation speed (A.3 and A.4).

The molten polymer is considered as behaving as a generalized Newtonian fluid with the viscosity described by the Cross model:

$$\eta(\dot{\gamma}) = \frac{\eta_r}{1 + (\eta_r \dot{\gamma} / \tau^*)^{1-n}} \quad (9)$$

where model constants take on values corresponding to polystyrene at 200 °C [21,30]: $n = 0.26$, $\tau^* = 2.5 \times 10^4$ Pa, $\eta_r = 3.841 \times 10^3$ Pa s.

Fig. 6 shows the computational domain for the two screw elements considered, with the fluid region being shown in transparent gray. A cross-section of the grid at $x = L/2$ is also shown. The conveying element is a right-handed full flight screw, whereas the mixing screw element is a similar right-handed screw with left-handed slots. The flight length of the slots is twice that of the base element. The mesh has a total of 595,455 nodes and 2,870,400 tetrahedral elements. Both screws rotate anti-clockwise at angular speed ω and the polymer enters the domain in the positive x direction. The geometry of the screws is indicated in a cross section in Fig. 7. The barrel radius is $R = 10.15$ mm, while the screw dimensions are $R_1 = 10$ mm, $R_2 = 6.25$ mm and $d = 3$ mm. The distance between the centers of rotation of the two screws is $\Delta z = 8.2$ mm and the screw element length is $L = 20$ mm (one complete screw flight). The computational domain contains one region at the entry of the flow and another at the exit where no flights are present. The remaining cylinder in these regions has a radius equal to the smallest radius of the screw elements (R_2).

The level-set functions determining the volume occupied by each screw are computed using analytical functions. Say $\psi_0(y, z, \theta)$

is a level-set function such as $\psi_0 = 0$ represents the surface of the conveying screw in a given section, where θ is the angle between the screw profile axes in the respective section and the fixed reference frame. As an example, for the two screw profiles shown in Fig. 7, the angle θ is $\pi/2$ for the screw shown on the right hand side and $\theta = 0$ for the screw on the left hand side. The screw profile is the same in any cross section but corresponds to a different rotation angle θ , so $\psi_0(y, z, \theta)$ can be obtained from the screw profile at $\theta = 0$ by simply using

$$\psi_0(y, z, \theta) = \psi_0(y^*, z^*, 0) \quad (10)$$

where $y^* = y \cos(\theta) + z \sin(\theta)$ and $z^* = -y \sin(\theta) + z \cos(\theta)$. The screw surfaces are then determined by using the following formulas:

$$\psi_1(x, y, z, t) = \psi_0(y, z - \Delta z/2, \theta_1(x, t)) \quad (11)$$

$$\psi_2(x, y, z, t) = \psi_0(y, z + \Delta z/2, \theta_2(x, t)) \quad (12)$$

with

$$\theta_1(x, t) = -\pi \left(\frac{x}{L} - \frac{1}{2} \right) + \omega t \quad (13)$$

$$\theta_2(x, t) = -\pi \frac{x}{L} + \omega t \quad (14)$$

and where ω is the angular speed of rotation of the screws (ω takes on positive values for screws rotating anti-clockwise). The function ψ_1 corresponds to the screw on the right hand side of Fig. 7, having the center located at $z = \Delta z/2$, while the function ψ_2 corresponds to the screw on the left hand side of Fig. 7. Both level-set functions will take negative values inside the volume occupied by the respective screw and are positive in the fluid region. The level-set function representing both screws is constructed by simply taking

$$\psi = \min(\psi_1, \psi_2). \quad (15)$$

This simple and fast procedure is employed to recompute the level-set function at mesh nodes for each time step, then the IB-BCE method described in Section 2.4 is used to impose the screw speed on the immersed boundary. Note that by using analytical functions to determine the level-set function describing the solid boundary, instead of solving a transport equation, we avoid integration errors resulting in undesired artificial dissipation.

Table 3
Mesh information for grid dependence study.

Mesh	# Of nodes	# Of elem.	# Of elem. axial in + screw + out	# Of elem. circumferential	# Of elem. radial
1	86,867	406,640	6 + 40 + 6	46	17
2	255,881	1,219,920	9 + 60 + 9	68	23
3	595,455	2,870,400	12 + 80 + 12	92	30

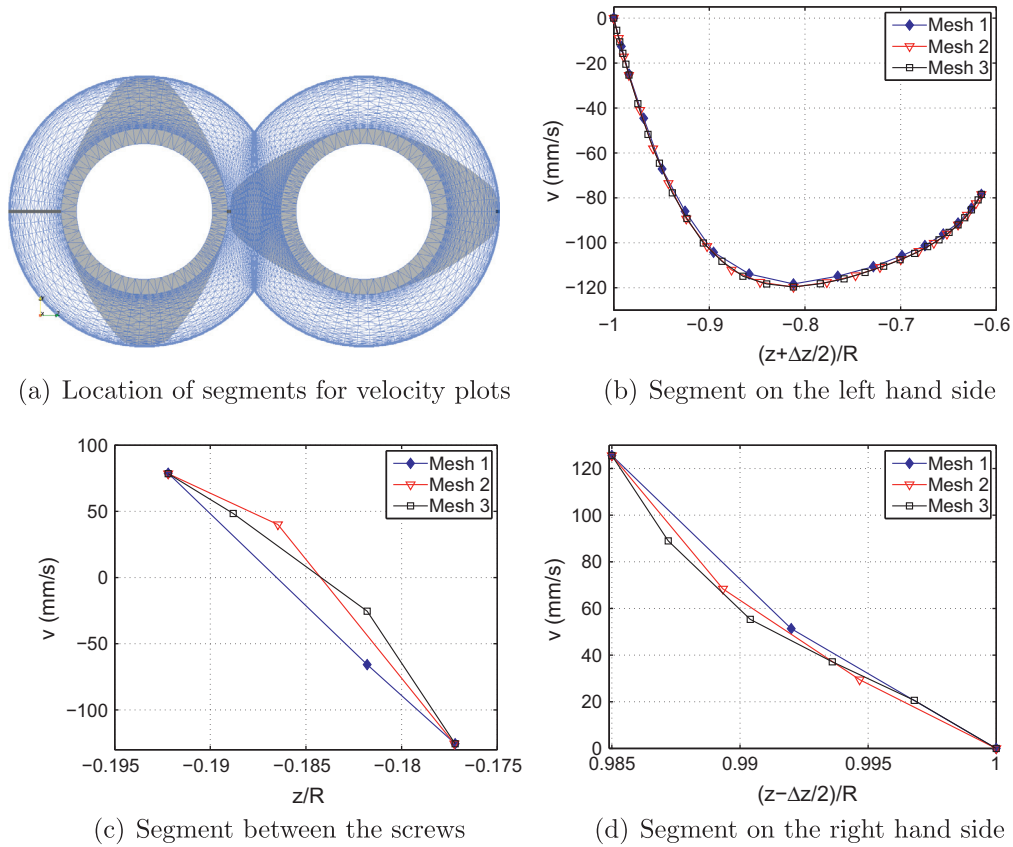


Fig. 8. Effect of grid refinement on velocity v at $x = L/2$ and $y = 0$.

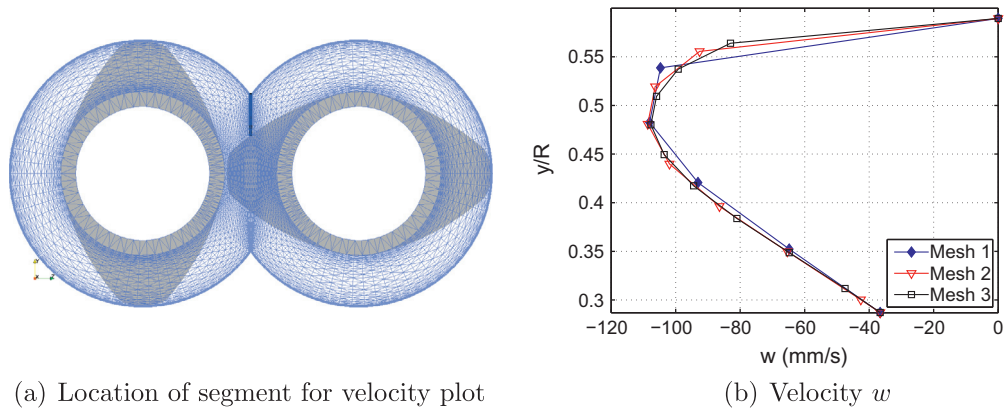


Fig. 9. Effect of grid refinement on velocity w at $x = L/2$ and $z = 0$.

First, the dependence of the flow solution on mesh refinement is assessed for the conveying elements rotating at 120 RPM. Computations were carried out on the meshes described in Table 3.

The velocity profile along the horizontal line $x = L/2$, $y = 0$ is plotted in Fig. 8. As shown in Fig. 8a this line crosses the fluid region at three distinct locations: one segment on the left hand side of the computational domain, one segment between the two screws and a third segment on the thin gap between the right hand side screw and the barrel. In all three graphs the symbols correspond to values at mesh nodes, thus indicating the level of refinement at various locations inside the flow. For example in the thin gap on the right hand side of the barrel, corresponding to Fig. 8d, Mesh 1 has one node between the screw surface and the barrel,

Mesh 2 has two nodes and Mesh 3 has four nodes. Note that the nodes at $(z - \Delta z/2)/R = 1$ are on the surface of the barrel, whereas the points at $(z - \Delta z/2)/R = 0.985$ are the additional degrees of freedom corresponding to the immersed screw boundary and where the screw velocity is imposed. Inside the larger space on the left hand side of the domain, Fig. 8b, the solution changes little between meshes 1 and 2 and then the solutions are almost the same for meshes 2 and 3. At the other two locations the velocity exhibits rapid variations inside very thin spaces where a limited number of mesh nodes are found. However, the velocity gradient does not change significantly and solutions on meshes 2 and 3 are close one to each other thus indicating that discretization errors on the final Mesh 3 are small.

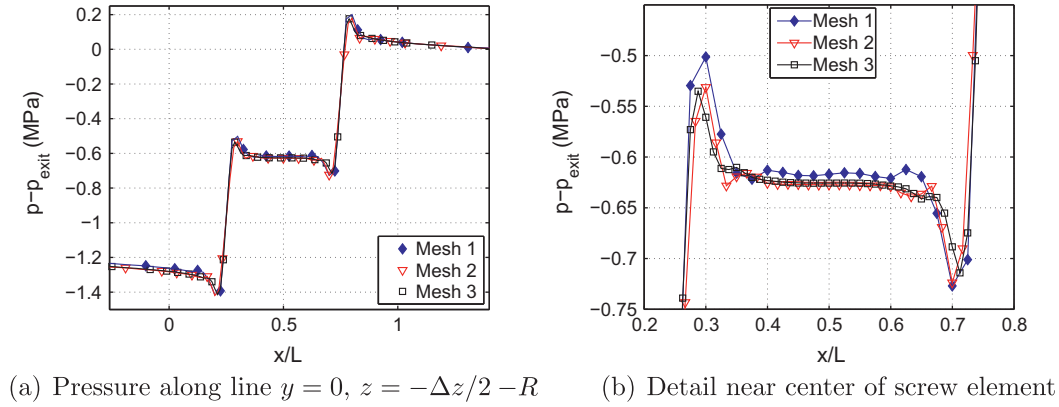


Fig. 10. Effect of grid refinement on the pressure along the barrel.

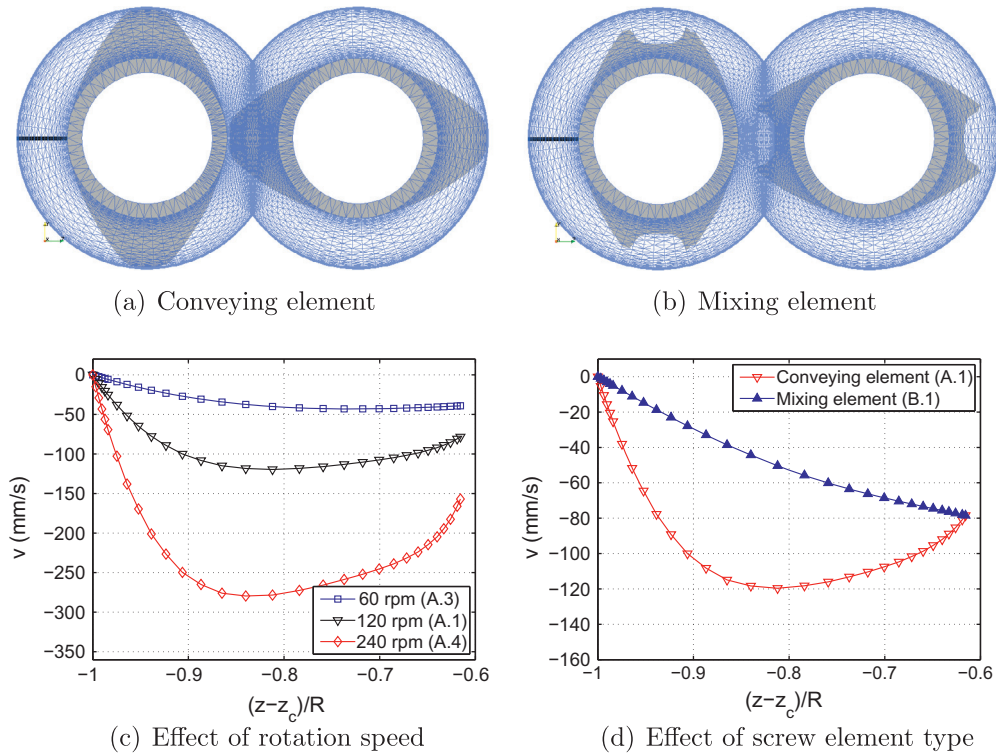


Fig. 11. Velocity v profile at $x = L/2$ and $y = 0$.

The velocity profile along the vertical line $x = L/2$, $z = 0$ is shown in Fig. 9. The segment along which the velocity is plotted is indicated in Fig. 9a. Here again the symbols in Fig. 9b indicate values at mesh nodes. Observe that larger differences are observed for the solution on Mesh 1 when compared to the solution on the other two meshes which are close one to each other. Differences between the solutions on meshes 2 and 3 are only observed near $y/R = 0.55$ where the flow passes over the corner made by the barrel surface and where higher velocity gradients are observed.

The pressure computed on the barrel surface along the line $y = 0$, $z = -\Delta z/2 - R$ is shown in Fig. 10. The solutions for the three meshes are compared in Fig. 10a for the entire length of the computational domain and a detail around the middle of the element screw is shown in Fig. 10b. The symbols represent nodal values in Fig. 10b, whereas in Fig. 10a only one in four nodes is indicated by symbols. The total pressure drop computed is 1.215 MPa on Mesh 1, 1.236 MPa on Mesh 2 and 1.235 MPa on Mesh 3. Hence,

the difference between meshes 1 and 3 is of 1.6%, whereas that between meshes 2 and 3 is of only 0.14%. This results indicate that the discretization errors are small for the solution on Mesh 3. This refined mesh is used in the computations discussed below.

In the remaining of this section we present the influence of the screw type, feed rate and screw rotation speed on the distribution of the velocity and pressure inside the polymer melt. Note that the inlet flow rate is much smaller when compared with the screw rotation speed and therefore has little influence on the velocity distribution (case A.2 compared to A.1 and case B.2 compared to B.1).

Fig. 11 shows the y -component of the velocity at $x = L/2$ and $y = 0$, while Fig. 12 shows the z -component of the velocity at $x = L/2$ and $z = 0$. The thicker lines on the pictures illustrating the screw cross-section and computational mesh indicate the locations where the velocities are plotted. The solutions for the conveying element at different rotation speeds (cases A.1, A.3 and A.4) are compared in Fig. 11c and in Fig. 12c, whereas the two type of screw

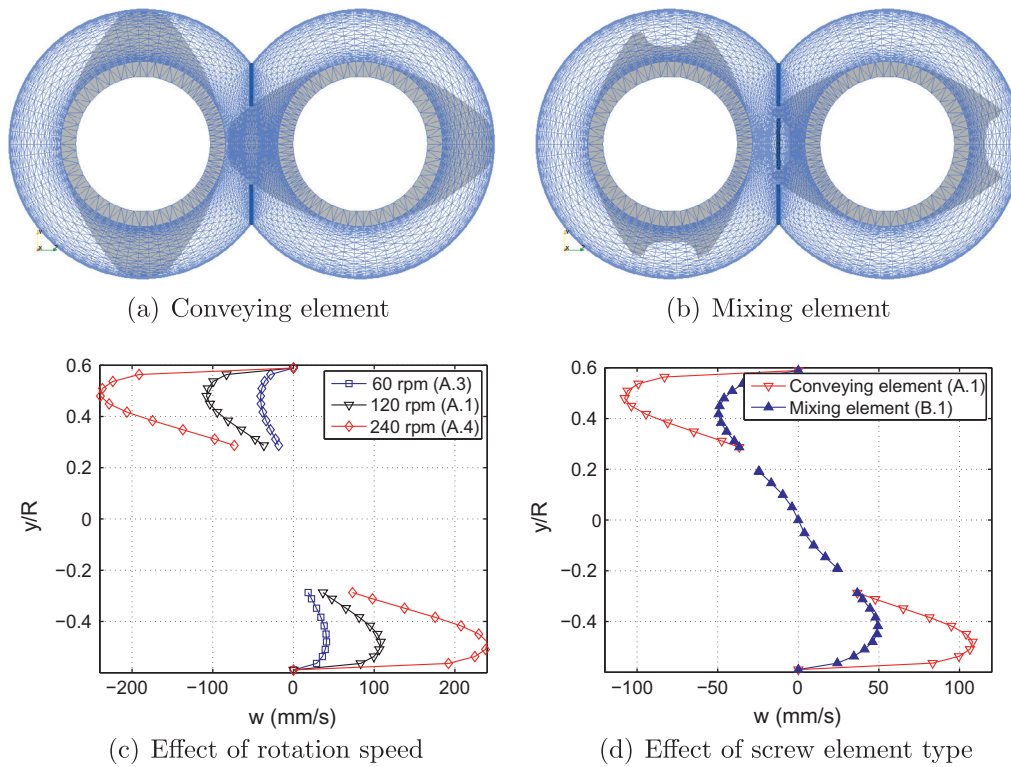
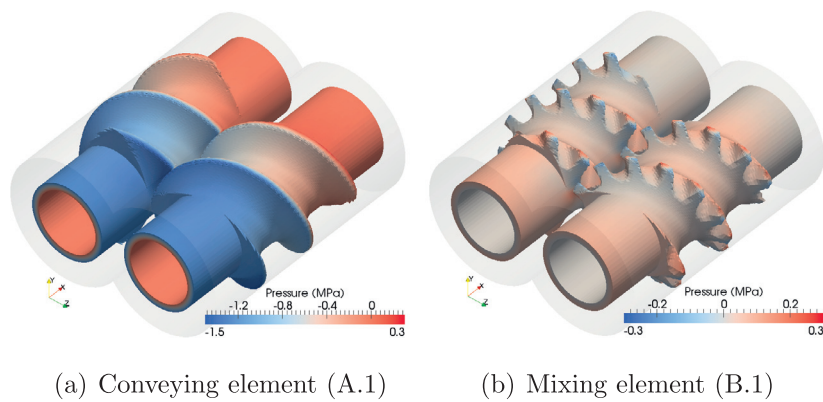
Fig. 12. Velocity w profile at $x = L/2$ and $z = 0$.

Fig. 13. Pressure distribution on the screws surface.

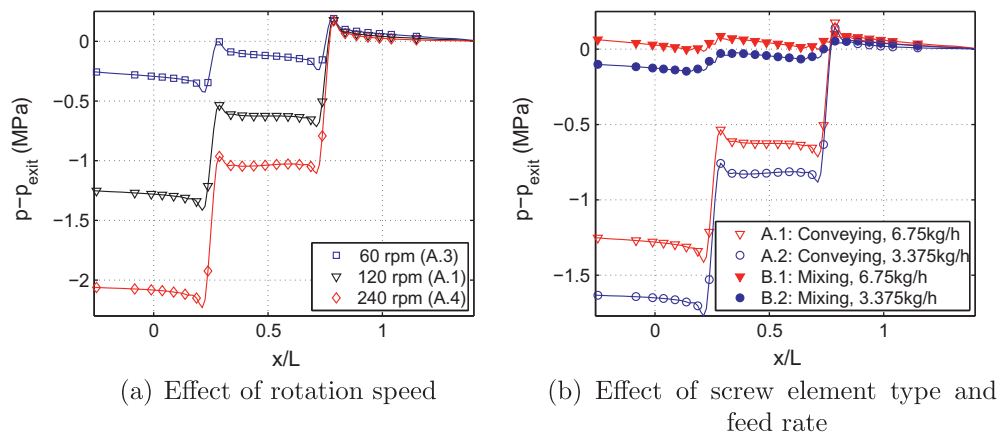


Fig. 14. Pressure along the barrel.

Table 4

Configuration of the 13 element screw.

Screw element type	Length (mm)
NO10/10	10
SE20/20	20
SE40/40	40
2SE30/30	60
SME20/20	20
SE20/20	20
SME20/20	20
2SE40/40	80
2SE30/30	60
2SE20/20	40
NO10/10	10

elements at 120 RPM are compared in Fig. 11d and in Fig. 12d. The maximum velocity increases by a factor larger than 2 when the rotation speed increases two fold as a result of the shear thinning behavior of the material. This is more evident for the v -velocity in Fig. 11c for which the shape changes when the rotation speed increases from 60 to 240 RPM, the maximum velocity increasing by a factor of six. As can be seen in Figs. 11d and 12d the velocity profile changes dramatically between the conveying and mixing screw elements, with the velocity amplitude being much smaller in the case of the mixing element.

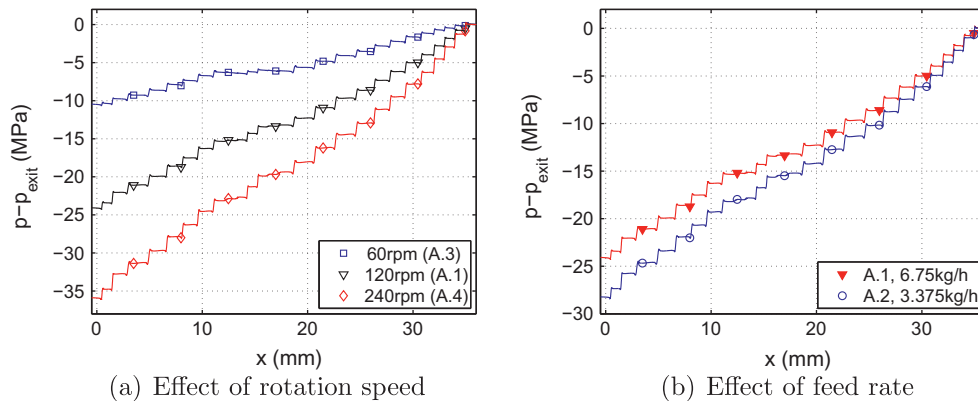
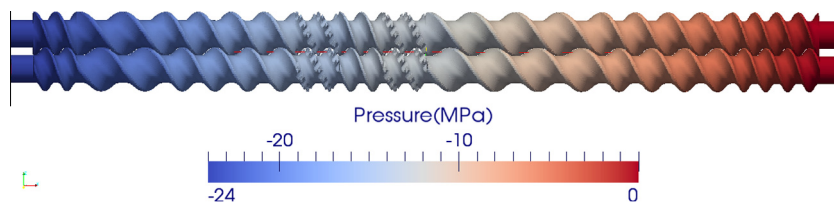
The pressure distribution on the surface of the two screws for cases (A.1) and (B.1) is shown in Fig. 13. Note that the exit pressure is taken as a reference and it was fixed to 0 in the numerical simulation. The magnitude of the pressure changes along the screw is much more important for the conveying element as the openings present in the mixing element allows a back flow. The pressure evolution on the surface of the barrel along the line $y=0$, $z=-\Delta z/2-R$ for various operating conditions is shown in Fig. 14. Fig. 14a indicates an increase in the magnitude of the pressure change along the screw when the rotation speed increases as the larger velocities more than offset the decrease in the viscosity. The influence of the feed rate and of the screw element type is shown in Fig. 14b. Pressure changes are much smaller for the

mixing element than for the conveying element. Note also that the pressure increase along the screw element is larger for the smaller feed rate. This is determined by the fact that a higher flow rate is associated with a higher upstream pressure. On top of that we have the pressure changes determined by the screw rotation which generates an increase of the pressure in the flow direction.

3.3. Flow inside a 13 element twin-screw extruder

In this section solutions are shown for the flow inside a 13 element twin-screw extruder using the same viscosity model as in the previous section. The screw is 380 mm in length and consists of a series of conveying and mixing elements with different screw flight as shown in Table 4. The name of each section should be interpreted as follows: the letters identify the type of element (NO for no screw, SE for conveying elements and SME for mixing elements) followed by two numbers with the first indicating the length of the element (in mm) and the second indicating the screw flight of the respective element (in mm). Where more than one element of the same type are placed in succession, the number of elements is indicated in front of the element type. The NO screw regions are identical to the regions at the beginning and end of the computational domain used in the previous section. Note also that the screw elements investigated in the previous section are the SE20/20 element for the conveying element and SME20/20 for the mixing element. The screw profile remains the same along the entire length of the screw.

The mesh in this case has a total of 6,113,338 nodes and 29,725,200 tetrahedral elements. Simulations were carried out for the same screw rotation speed and feed rate as those of cases A.1–A.4. Hence, both the effect of changing the screw rotation speed (cases A.3 and A.4 compared with A.1) and feed rate (case A.2 compared with A.1) were considered. As for the single screw element, the pressure change along the screw increases with increasing screw rotation speed and also increases when decreasing the feed rate (see Fig. 15). Remark also that the pressure drop along each conveying element is almost the same, whereas much

**Fig. 15.** Pressure along the barrel for the 13 element screw.**Fig. 16.** Pressure at the surface of the entire screw for condition A.1.

smaller pressure variations are observed along mixing elements. This observation is in agreement with the results for the single screw elements presented in the previous section. The pressure distribution along the entire screw surface is shown in Fig. 16 for the conditions A.1. The polymer melt is pushed from left to right by the screws rotation and the maximum pressure is recovered at the right end of the computational domain. The pressure varies gradually along conveying elements and much smaller changes in the pressure are observed in the region of mixing elements.

4. Conclusions

This work presents the application of an IB-BCE method to study flow inside co-rotating twin-screw extruders. The IB finite element method accurately imposes the boundary conditions on the fluid/solid interface. The procedure incorporates into the grid the points where the mesh intersects the boundary. The degrees of freedom associated with the additional grid points are then eliminated either because the velocity is known or by static condensation in the case of the pressure. Application to the flow around an array of spheres indicated that the proposed method is accurate and very sensitive to the position of the fluid/solid interface.

For the flow inside a twin screw extruder the polymer melt is considered to behave as a generalized Newtonian fluid and flow solutions indicate that velocity profiles are affected by the shear thinning behavior of the material. The pressure drop along the screw depends on the screw rotation speed, feed rate and screw type. The pressure buildup between the exit and entry of a screw element increases when increasing the screw rotation speed and is much more important for a conveying element than for a mixing element.

The 3D solution algorithm was then used to compute the flow inside a 13 element screw formed by several conveying and mixing elements. Solutions are shown for different screw rotation speeds and feed rates and the same behavior is observed as for single screw elements. The pressure drop is larger for the conveying elements than for mixing elements and increases with increasing screw rotation speed.

The advantage of using the IB-BCE method for computing the flow inside twin screw extruders is more significant when analyzing the mixing behavior of different screw elements and when including heat transfer solution. Such problems involve convective transport and coupling between solutions at different time steps for which the fact that a single mesh is used over the entire computation is a great advantage: no interpolation between different meshes is needed for the present approach. These topics of special interest to the plastic industry are presently under investigation and will be the object of a future publication.

References

- [1] Mittal R, Iaccarino G. Immersed boundary methods. *Annu Rev Fluid Mech* 2005;37:239–61.
- [2] Löhner R, Cebal JR, Camelli FE, Appanaboyina S, Baum JD, Mestreau EL, et al. Adaptive embedded and immersed unstructured grid techniques. *Comput Methods Appl Mech Eng* 2008;197:2173–97.
- [3] Löhner R, Appanaboyina S, Cebal JR. Comparison of body-fitted, embedded and immersed solutions of low Reynolds-number 3-D incompressible flows. *Int J Numer Methods Fluids* 2008;57:13–30.
- [4] Ilinca F, Héty J-F. A finite element immersed boundary method for fluid flow around rigid objects. *Int J Numer Methods Fluids* 2011;65:856–75.
- [5] Ilinca F, Héty J-F. A finite element immersed boundary method for fluid flow around moving objects. *Comput Fluids* 2010;39:1656–71.
- [6] Ilinca F, Héty J-F. Solution of flow around complex-shaped surfaces by an immersed boundary-body conformal enrichment method. *Int J Numer Methods Fluids* 2012;69:824–41.
- [7] Speur JA, Mavridis H, Vlachopoulos J, Janssen LPBM. Flow patterns in calender gap of a counterrotating twin screw extruder. *Adv Polym Technol* 1987;7:39–48.
- [8] Kajiwar T, Nagashima Y, Nakano Y, Funatsu K. Numerical study of twin-screw extruders by three-dimensional flow analysis – development of analysis technique and evaluation of mixing performance for full flight screws. *Polym Eng Sci* 1996;36(16):2142–52.
- [9] Bravo VL, Hrymak AN, Wright JD. Numerical simulation of pressure and velocity profiles in kneading elements of a co-rotating twin screw extruder. *Polym Eng Sci* 2000;40:525–41.
- [10] Bertrand F, Thibault F, Delamare L, Tanguy PA. Adaptive finite element simulations of fluid flow in twin-screw extruders. *Comput Chem Eng* 2003;27:491–500.
- [11] Cheng H, Manas-Zloczower I. Study of mixing efficiency in kneading discs of co-rotating twin-screw extruders. *Polym Eng Sci* 1997;37:1082–90.
- [12] Cheng H, Manas-Zloczower I. Distributive mixing in conveying elements of a ZSK-53 co-rotating twin screw extruders. *Polym Eng Sci* 1998;38:926–35.
- [13] Yao C-H, Manas-Zloczower I. Influence of design on dispersive mixing performance in an axial discharge continuous mixer – LCMAX 40. *Polym Eng Sci* 1998;38(6):936–46.
- [14] Zhang X-M, Feng L-F, Chen W-X, Hu G-H. Numerical simulation and experimental validation of mixing performance of kneading discs in a twin screw extruder. *Polym Eng Sci* 2009;49(9):1772–83.
- [15] Ishikawa T, Kihara S-I, Funatsu K. 3-D Numerical simulations of nonisothermal flow in co-rotating twin screw extruders. *Polym Eng Sci* 2000;40:357–64.
- [16] Malik M, Kalyon DM. 3D Finite element simulation of processing of generalized Newtonian fluids in counter-rotating and tangential TSE and die combination. *Int Polym Process* 2005;20:398–409.
- [17] Kalyon DM, Malik M. An integrated approach for numerical analysis of coupled flow and heat transfer in co-rotating twin screw extruders. *Int Polym Process* 2007;22:293–302.
- [18] Noble DR, Newren EP, Lechman JB. A conformal decomposition finite element method for modeling stationary fluid interface problems. *Int J Numer Methods Fluids* 2010;63:725–42.
- [19] A.S. Fard, M.A. Hulsen, P.D. Anderson, Extended finite element method for viscous flow inside complex three-dimensional geometries with moving internal boundaries. *Int J Numer Methods Fluids*, in press. <http://dx.doi.org/10.1002/fld.2715>.
- [20] Codina R, Houzeaux G, Coppola-Owen H, Baiges J. The fixed mesh ALE approach for the numerical approximation of flows in moving domains. *J Computat Phys* 2009;228:1591–611.
- [21] Ilinca F, Héty J-F. Three-dimensional finite element solution of the flow in single and twin-screw extruders. *Int Polym Process* 2010;25:275–86.
- [22] T.E. Tezduyar, R. Shih, S. Mittal, S.E. Ray, Incompressible flow using stabilized bilinear and linear equal-order-interpolation velocity–pressure elements, Research Report UMSI 90/165, University of Minnesota/Supercomputer Institute, Minneapolis, 1990.
- [23] Ilinca F, Pelletier D, Garon A. An adaptive finite element method for a two-equation turbulence model in wall-bounded flows. *Int J Numer Methods Fluids* 1997;24:101–20.
- [24] Franca LP, Frey SL. Stabilized finite element methods: II. The incompressible Navier–Stokes equations. *Comput Methods Appl Mech Eng* 1992;99(2–3):209–33.
- [25] Karypis G, Kumar V. A parallel algorithm for multilevel graph partitioning and sparse matrix ordering. *Parall Distrib Comput* 1998;48:71–85.
- [26] Saad Y. Iterative methods for sparse linear systems. Boston (MA): PWS Publishing Company; 1996.
- [27] Van der Vorst H. Bi-CGSTAB: a fast and smoothly converging variant of Bi-CG for the solution of nonsymmetric linear systems. *SIAM J Sci Stat Comput* 1992;13:631–44.
- [28] Martys NS, Hagedorn JG, Goujon D, Devaney JE. Large scale simulations of single and multi-component flow in porous media. In: Proceedings of SPIE conference on developments in X-ray tomography IISPIE, vol. 3772; 1999. p. 205–13.
- [29] Chapman AM, Higdon JLL. Oscillatory Stokes flow in periodic porous media. *Phys Fluids A* 1992;4:2099–116.
- [30] Ilinca F, Héty J-F. Three-dimensional filling and post-filling simulation of polymer injection moulding. *Int Polym Process* 2001;16:291–301.